

Full length article

Rapid supersonic spraying of Cu(In,Ga)(S,Se)₂ nanoparticles to fabricate a solar cell with 5.49% conversion efficiency



Jung-Jae Park^{a,1}, Jong-Gun Lee^{a,1}, Do-Yeon Kim^a, Jong-Hyuk Lee^a, Jae Ho Yun^b, Jihye Gwak^b, Young-Joo Eo^b, Ara Cho^b, Mark T. Swihart^c, Salem S. Al-Deyab^d, Sejin Ahn^{b,**}, DongHwan Kim^e, Sam S. Yoon^{a,*}

^a School of Mech. Eng., Korea University, Seoul 136-713, Republic of Korea

^b Solar Energy Research Department, Korea Institute of Energy Research, Daejeon 305-343, Republic of Korea

^c Department of Chemical and Biological Engineering, University at Buffalo, The State University of New York, Buffalo, NY 14260-4200, USA

^d Petrochemicals Research Chair, Department of Chemistry, College of Science, King Saud University, Riyadh 11451, Saudi Arabia

^e Department of Materials Science and Engineering, Korea University, Seoul 136-713, Republic of Korea

ARTICLE INFO

Article history:

Received 23 June 2016

Received in revised form

10 October 2016

Accepted 10 October 2016

Keywords:

CIGS nanoparticle

Supersonic flow

Kinetic spray

CIGS film

Impact bonding

ABSTRACT

We demonstrate production of high-quality Cu(InGa)(SSe)₂ (CIGS_{Se}) films by high-rate supersonic spray deposition. This technique is unique in creating particle-based films without introducing impurities, because no additives or binders are used. The thin film deposition process was investigated computationally, to understand the pulverization of the incoming particles. These simulations were consistent with experimental observations. Grain growth was improved by adding a 300-nm copper layer atop the CIGS_{Se} film; selenization of the resulting bilayer produced a CuSe liquid flux that assisted the sintering process. The final CIGS_{Se} film-based solar cell had a conversion efficiency of 5.49% with $J_{sc} = 18.73$ mA/cm², $V_{oc} = 0.488$ V, and $FF = 59.99\%$ in an active area of 0.44 cm².

© 2016 Acta Materialia Inc. Published by Elsevier Ltd. All rights reserved.

1. Introduction

Cu-In-Ga-Se (CIGSe) solar cells have attracted attention worldwide because they have excellent electronic and optical properties [1,2] such as a direct bandgap and high absorption coefficients. The best CIGSe thin-film solar cell yet reported has a conversion efficiency of 21.7% [3]. However, this high-efficiency CIGSe thin film was created using high vacuum techniques, such as co-evaporation and sputtering, which are difficult to apply in mass production. Fabrication of CIGSe films by expensive vacuum techniques has hindered the cost-competitive production of solar cells, and development of low-cost non-vacuum processes will be important in expanding the production of CIGSe solar cells [4–6].

Non-vacuum processes are typically based on solution-type precursors containing organic solvents and polymer binder

materials. These are directly deposited onto substrates via printing, electroplating, dip-coating, spraying, or spin-coating [7–9]. The organic additives and binders induce impurities, such as residual C, in the final CIGSe film after annealing [10,11]. Residual C-containing compounds have been reported to cause high series resistance in photovoltaic devices, as well as poor interfacial adhesion between CIGSe films and the typical Mo substrate [10,11]. To overcome this residue-related problem, a hydrazine-based solution process was introduced for CIGS film deposition, with a reported efficiency of 15.2% [12–15]. However, hydrazine is both highly toxic and explosive, hindering its use in industrial-scale mass production. The C-containing layers can also be removed by multi-step heat treatment processes [16]; however, the complete removal of impurities by this method seems to be impossible [17].

The solution processes also suffer from inefficient layer packing, which hinders intergranular cohesion and interlayer adhesion. Poor cohesion and adhesion generate pores and cracks in the final film, which can generate shunt currents that eventually reduce the open-circuit voltage (V_{oc}) and fill factor (FF). To circumvent these challenges, Eldada et al. [18] suggested a reactive transfer printing

* Corresponding author.

** Corresponding author.

E-mail addresses: swisstel@kier.re.kr (S. Ahn), skyoona@korea.ac.kr (S.S. Yoon).

¹ These authors have contributed equally.

method. Lim et al. [19] demonstrated the use of cold-isostatic pressing (CIP), which densified the absorber layer and improved the microstructure of Cu-In-Se (CISe) films. However, the additional processes necessary for physical and cold-isostatic pressing appear to be both complex and expensive. A simple deposition method is still required to realize the low-cost production of thin-film solar cells.

We introduce a supersonic spray-coating technique for the fabrication of Cu(InGa)(SSe)₂ (CIGSSe) thin films under low vacuum conditions. The technique can be extended to roll-to-roll processing and has the advantages of using pure dry CIGSSe particles without binders or additives, rapidly producing films in tens of seconds to a few minutes, dense and compact layer formation from supersonic impact and pulverization, and potential scalability by using multiple spray nozzles and roll-to-roll processing.

Supersonic kinetic spraying is traditionally utilized for the fabrication of ceramic layers such as Pb(Zr,Ti)O₃, α -Al₂O₃, Y₂O₃, YSZ, AlN, and MgB₂ [20]. To the best of our knowledge, the technique has not yet been used for the thin-film fabrication of CIGSSe. In a previous study, we computationally investigated the thin-film deposition process of CIGSSe particles by supersonic spraying and explored the possibility of producing films experimentally [21]. Herein, we compare the numerical simulation of the thin film deposition process to real experimental results on fabrication and testing of a solar cell.

2. Experimental

2.1. Preparation of the CIGSe film

CIGSe powder (d_{50} ~177 μ m, compound atomic ratio 1 (Cu):1 (In + Ga):2 (Se)) was purchased from *Changsha* (China). The CIGSe powder was crushed by a jet-mill system because the original particle size was too large to use in the kinetic spray system. This jet-mill process created CIGSe particles with an average size of ~0.8 μ m. The reduction in particle size was expected to improve the quality of the deposited films and decrease cracking or damage in the Mo substrate. Particle size was confirmed to be important in particle acceleration [21–25]. The prepared CIGSe particles were fed through the supersonic nozzle by a powder feeder and then accelerated by supersonic flow. The deposition chamber was evacuated to permit supersonic flow. The nozzle coated the Mo-coated glass substrate between two and eight times to form dense CIGSe films with thicknesses of ~0.8–2.5 μ m. The substrate was located 10 mm from the nozzle, which was installed onto a controllable x - y moving stage that could move at a maximum rate of 12.5 mm/s. The deposition coating time to generate a ~1.0- μ m-thick CIGSe film was ~10 s. The substrate was heated and maintained at 200 °C during spraying. The as-deposited CIGSe films were cleaned by N₂ gas to remove residual particles from the film surfaces.

2.2. Post-processing

Heat treatment under H₂S was found to remove O from the as-deposited CIGSe film. The O was trapped within the film because air was used as the carrier gas to make the films [17]. The as-deposited CIGSe films were annealed at 500 °C for 20 min with a ramp-up speed of 25 °C/min in the H₂S (1%)/N₂ gas flow, with a flow rate maintained at 100 sccm. The selenization of the CIGSe film was performed using rapid thermal processing (RTP) in a quartz tube. We fabricated a custom container for stable selenization, made of quartz and consisting of three layers. The CIGSe film was placed on the bottom layer; a porous graphite plate was placed in the middle layer. Then Se powder

(Sigma-Aldrich, 0.07 g) was distributed evenly on the graphite plate. The container was covered with a quartz plate to prevent the leakage of Se gas. The RTP furnace for selenization was closed and purged with N₂ gas to prevent the undesired oxidation of the CIGSe film. A schematic of the selenization process is presented in Fig. S1.

2.3. Cell fabrication

The solar cells were fabricated with a conventional Mo/CIGSSe/CdS/ i -ZnO/ n -ZnO/Ni/Al structure. Mo-coated soda-lime glass was used as the substrate, where the Mo coating of ~1.0 μ m in thickness was deposited by DC magnetron sputtering. The CdS buffer layer of 60 nm in thickness was prepared on a CIGSSe absorber by chemical bath deposition (CBD), and transparent conducting oxide layers of i -ZnO (50 nm)/Al-doped ZnO (400 nm) were deposited by radio-frequency magnetron sputtering. The Al grid (1.6 μ m) was prepared by thermal evaporation as the current collector. The active area of the completed cell was 0.44 cm².

2.4. Characterization

The morphologies, compositions, and crystalline structures of the precursor films and the selenized films were investigated by high-resolution scanning electron microscopy (HRSEM, XL30SFEG Phillips Co., The Netherlands, 10 kV), energy dispersive spectroscopy (EDS, EDAX Genesis Apex, acceleration voltage, 30 kV; collection time, 100 s; with a standardless method), and X-ray diffraction (XRD, Rigaku Japan, D/MAX-2500, with Cu K α radiation), respectively. The compositional profile and the depth of the selenized film were determined by Auger electron spectroscopy (AES, PerkinElmer, SAM4300). The powder and films were structurally characterized by transmission electron microscopy (TEM, FEI Co., Tecnai F20) and FIB (FEI Helios NanoLab 600, USA). Device performance, characterized by the conversion efficiency and the external quantum efficiency (EQE), were measured with a class AAA solar simulator (WXS-155S-L2, WACOM, Japan) under AM1.5 conditions.

3. Results and discussion

Fig. 1 schematically shows the kinetic spray-coating technique used for CIGSe particle deposition. The kinetic spray system consists of a gas tank, powder feeder (Praxair 1264i, USA), supersonic nozzle, vacuum chamber, 2D x - y stage, booster pump, and vacuum pump. CIGSe powder is fed and accelerated into a de Laval nozzle with an air injection pressure of $P_0 = 2$ bar and gas temperature of T_0 , defined as room temperature of 25 °C. More details on the experimental setup are available in the referenced literature [26–29]. The operating conditions of the kinetic spray system are summarized in Table 1.

3.1. Modeling

In the experiment, the speed of CIGSe particle impact on the substrate could not be measured, because the particle velocity, accelerated by supersonic flow, was too high. For this reason, Ansys Autodyn simulations were performed to study the collision of high-speed CIGSe particles with the Mo substrate. AUTODYN is commonly used to study a wide variety of explosion and impact processes [30]. The simulation models were validated in our previous study [21] and the impact phenomena of single and multiple (18 simultaneous) CIGSe particles were investigated. In this study, we prepared a simulation with 90 CIGSe particles of non-spherical shapes to the process of formation of the dense CIGSe thin film. The

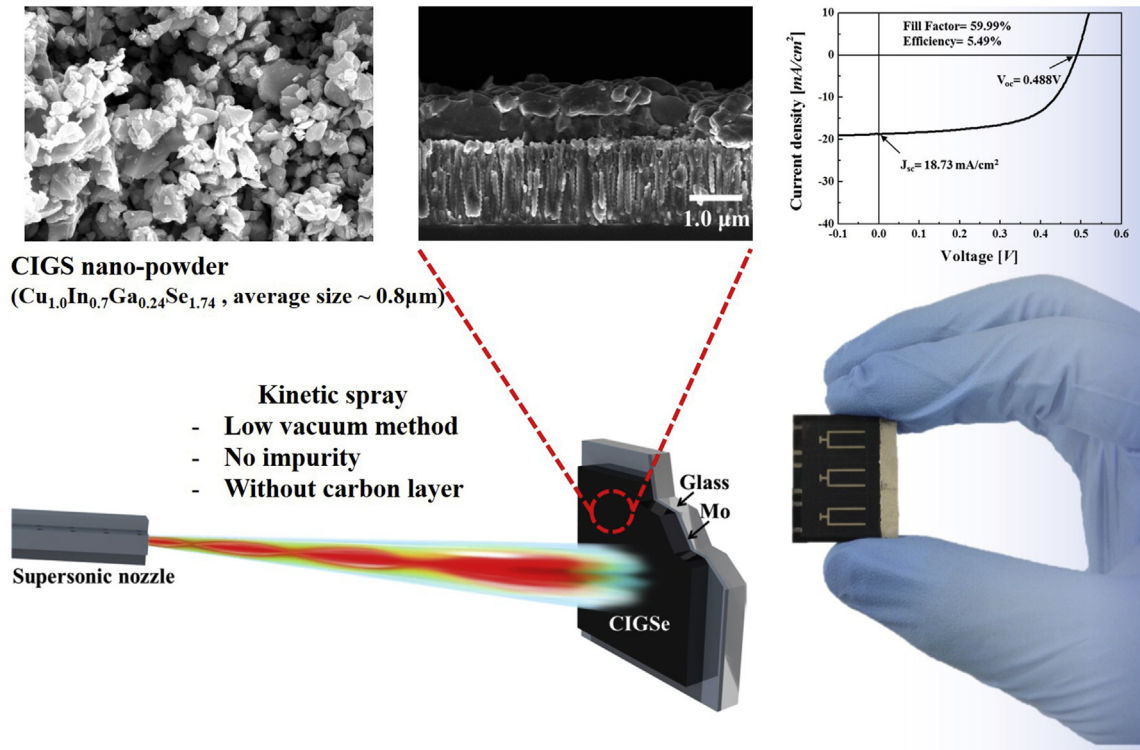


Fig. 1. Schematic of kinetic spray-coating process.

materials models used in simulation to the particle impact on the substrate and the coating mechanism are summarized in the [Supporting Information](#).

Many previous studies [31–34] have investigated single- and multiple-particle impact using spherical particle shapes in simulations. However, in reality, particles are not spherical but irregular in shape. In the simulation of the experiment, the CIGSe particles were set with hexagonal shapes of 0.8 and 1.2 μm height and width, respectively. In order to simulate the coating process depending on the path of motion, the distance between the particles was 0.5 μm and the 90 particles were distributed at an angle of 30° relative to the substrate surface. The number of finite elements per each particle was set to 630. The total number of elements in the substrate was set to 504,000. The substrate was a double layer of Mo-coated soda-lime glass. During the kinetic spraying, the CIGSe particle velocity was calculated by the self-selective method of particle velocity [35] and was ~ 200 m/s, exceeding the critical impact velocity of 150 m/s [32]. From our previous study, we knew that the particle velocity of ~ 200 m/s could form a CIGSe thin film without damaging the Mo substrate [21].

Table 1
Operating conditions of kinetic spray.

Pressure in deposition chamber [torr]	0.4
Propellant gas	Air
Powder	CIGSe
Particle velocity [m/s]	200
Stand-off distance [mm]	10
Gas temperature [K]	300
Substrate temperature [K]	473
Consumption of propellant gas [l/min]	3–8
Traverse speed [mm/s]	12.5
Number of passes	2–8

3.2. Multiple-particle impact

Fig. 2 presents the impact of the simulated CIGSe particles on the Mo substrate over a period t of 80 ns in two-dimensional space, where t is the impact time. The results show that the irregular CIGSe particles make impact with the Mo substrate and form a dense film. The impacted particles are pulverized and compressed by other particles to form a film of CIGSe on the substrate. The highest temperature $T_{\text{max}} = 1266$ K is observed at the interface between the particles. This temperature is lower than the 1300 K melting temperature of CIGSe [36]. Therefore, melting is not predicted to occur due to the thermal energy generated during the collision of the particles with the substrate. However, the heat generated by the impact of each particle improves the binding between the particles, forming a dense film with strong adhesion [32].

Fig. 3 compares the simulated particle impact at $t = 80$ ns (Fig. 2) and a cross-sectional scanning electron microscopy (SEM) image of the experimentally deposited CIGSe film. Fig. 3(a) and (b) confirms three results as follows: First, the particle speed ($V_p = 200$ m/s) does not damage the Mo substrate. This is important, as the Mo substrate acts as the back electrode for the solar cell; damage to it would directly affect the cell performance. Second, in the multiple-particle impact, the morphologies of the simulated and experimental pulverized particles are similar, as marked by the circles in Fig. 3. Third, a dense and adherent thin film is formed. The thermal energy provided by the impact of pulverized particles is sufficient to densify the film. To verify the density and the adhesion of deposited CIGSe thin films, we prepared two types of CIGSe films, using a 3-stage co-evaporation process and kinetic spraying, respectively. Scratch tests were performed on these CIGSe films using a revetest scratch tester (RST, CSM Instrument, Switzerland). A diamond needle tip with 100 μm radius moved 10 mm along the deposited CIGSe film with a normal force ranging from 1 to 10 N.

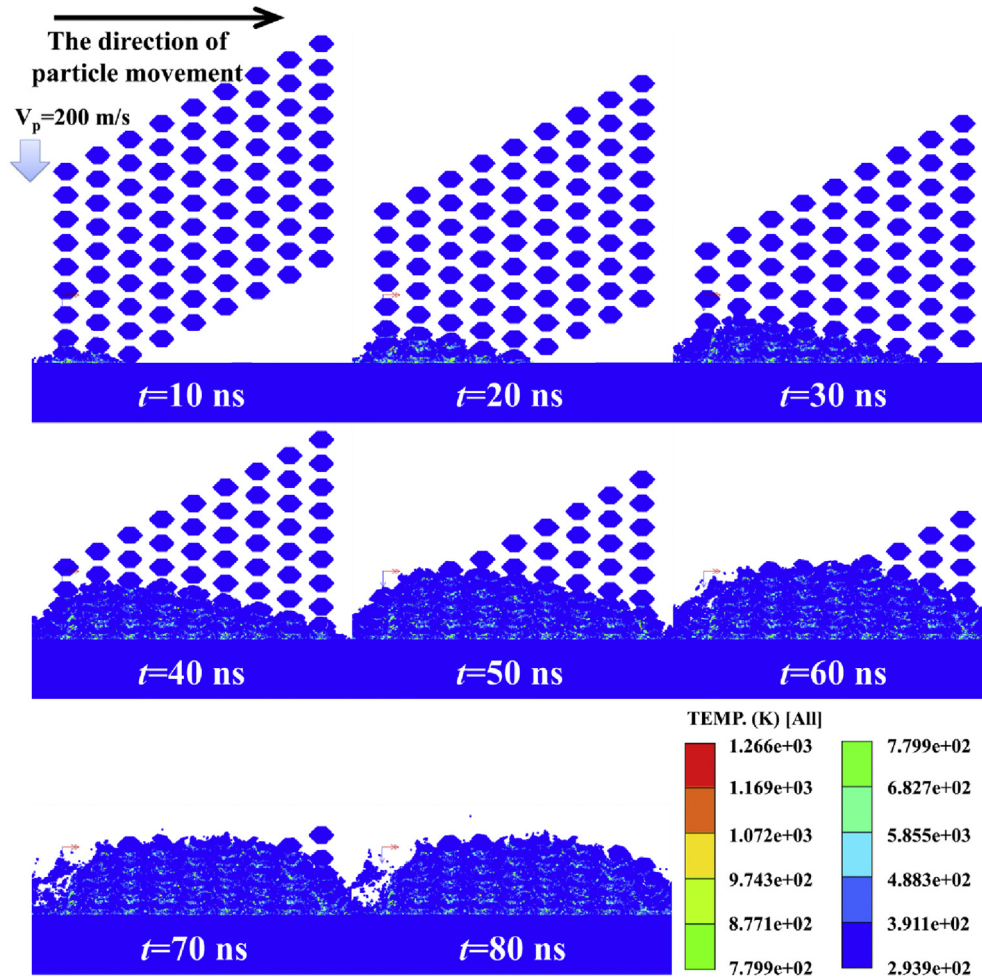


Fig. 2. Local temperature distribution of multiple CIGSe hexagonal particles impacting Mo substrate. (V_p is the particle velocity, t is impact time).

The needle was scanned at a strength rate of 2 N/min. The average values of critical load in the deposited CIGSe films prepared by 3-stage co-evaporation process and kinetic spray were determined to be 4.51N and 3.13N, respectively. Thus, the mechanical strength of the two films was similar. Qualitatively, the film deposited by kinetic spraying was more adherent to the Mo substrate than the film deposited by co-evaporation. This verifies that dense CIGSe thin films can be fabricated by kinetic spraying.

3.3. Analysis of CIGSe powder and as-deposited film

The CIGSe particle sizes were measured by a Mastersizer 3000

apparatus (Malvern, UK) with an average size of $\sim 0.8 \mu\text{m}$, as shown in Fig. 4(a). The inset is an SEM image of CIGSe particles crushed by jet-milling. As shown, the CIGSe powder particles are irregular in shape. The CIGSe particles were deposited on the Mo substrate by kinetic spraying to form a dense CIGSe thin film. An SEM image of the as-deposited CIGSe film is shown in Fig. 4(b), displaying uniformity and a thickness of $\sim 1.6 \mu\text{m}$.

In the jet-milling process, no impurities were formed, as verified by the X-ray diffraction (XRD) results presented in Fig. 5. Based on JCPDS #35-1102, the main XRD peaks at 26.92° , 44.68° , and 52.92° can be assigned to the (112), (220)/(204), and (312)/(116) faces, respectively, of the crystal structure of CIGSe [37,38]. The lattice

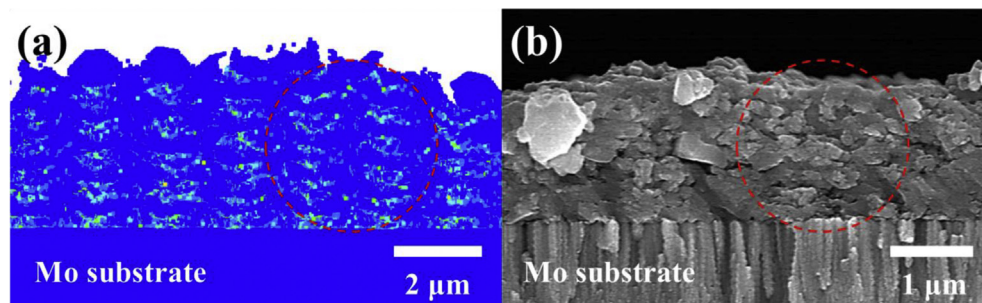


Fig. 3. (a) Simulated CIGSe thin film at $t = 80 \text{ ns}$ and (b) CIGSe thin film deposited by kinetic spray.

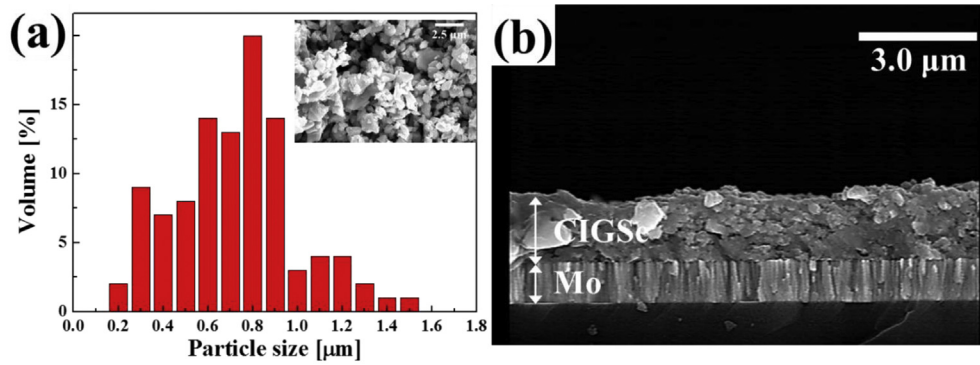


Fig. 4. (a) CIGSe particle size distribution (inset SEM image of CIGSe powder) and (b) SEM image of as-deposited CIGSe film by kinetic spray.

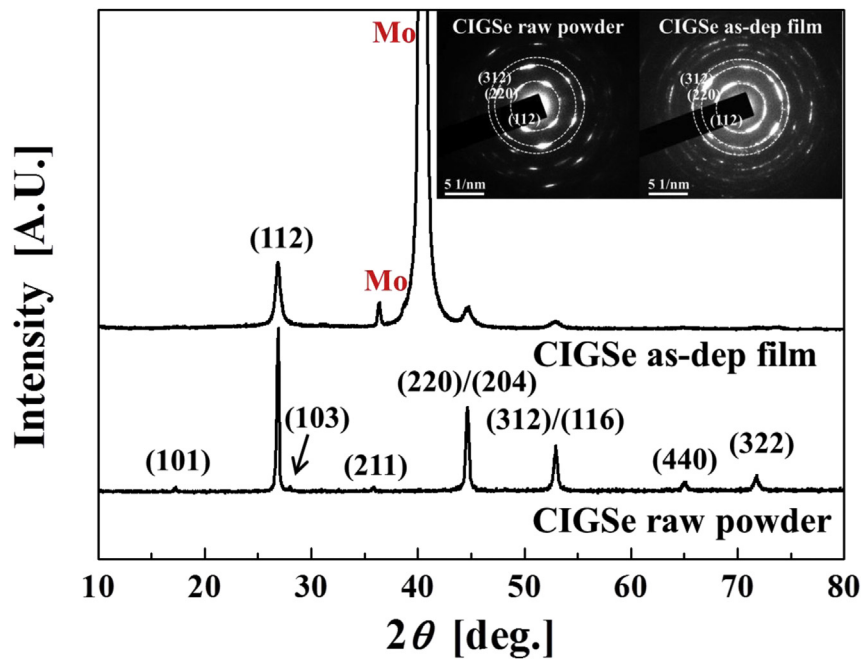


Fig. 5. X-ray diffraction (XRD) data of CIGSe raw powder and as-deposited film. Inset: transmission electron microscopy (TEM) selected area electron diffraction patterns of the CIGSe powder and film.

constants refined from the XRD data are $a = 5.723 \text{ \AA}$ and $c = 11.457 \text{ \AA}$, with $c/2a = 0.9997$. These lattice parameters and the $c/2a$ ratio calculated from the XRD data confirm that the crystal structure of the CIGSe particles was tetragonal chalcopyrite. Minor peaks at 17.12 , 28 , and 35.85° corresponding to the (101), (103), and (211) peak positions, respectively, are characteristic of the chalcopyrite structure [39]. The main peaks of the CIGSe film, correlating to the (112), (220)/(204), and (312)/(116) faces, are found in the pattern from the deposited film, matching that of the powder. This confirms that no phase transitions or formation of secondary phases occur during CIGSe film deposition. The crystallite sizes of the CIGS raw powder and as-deposited CIGSe film are summarized

Table 2
Lattice parameters of CIGS powder and as-deposited film at (112) peak.

Sample	Lattice parameter [Å]		Crystallite size [nm]
	a	c	
CIGSe raw-powder	5.723	11.457	33.7
as-dep CIGSe film	5.781	11.609	24.1

in Table 2. The broadening of the (112) peak of the CIGSe film compared to that of the raw powder confirms the decrease in crystallite size of the CIGSe film. The crystallite sizes of the CIGSe powder and as-deposited CIGSe film are 33.7 and 24.1 nm, respectively, as determined by the Debye-Scherrer relation. The crystallite size is decreased by fracturing upon high-velocity impact of the particles with the substrate in the kinetic spraying process [20,26,40]. These results are well matched with those from our previous study [21]. In order to further investigate the crystal structure of the CIGSe powder and as-deposited CIGSe film, selected-area electronic diffraction (SAED) patterns from TEM images are shown in the inset of Fig. 5. The SAED patterns of the CIGSe powder and as-deposited CIGSe film show the (112), (204), and (312) lattice planes, in agreement with the XRD data. The SAED patterns also show apparent hexagonal spots.

The composition of the CIGSe particles was analyzed by energy-dispersive X-ray spectroscopy (EDS). The results of the EDS analysis of the powder (not shown here) were averaged 10 times to determine a final composition of $\text{Cu}_{1.0}\text{In}_{0.7}\text{Ga}_{0.24}\text{Se}_{1.74}$. To confirm the composition of the as-deposited CIGSe film, we conducted EDS analysis, as presented in Fig. 6. For the EDS analysis, a $0.4\text{-}\mu\text{m}$ -thick

sample of the as-deposited CIGSe film was prepared to the requirements of the focused ion beam-SEM (FIB-SEM) apparatus. The cross-section of the as-deposited CIGSe film is characterized by the EDS line profile shown in Fig. 6(a). According to the EDS profile, the composition of the film is estimated to be $\text{Cu}_{1.0}\text{In}_{0.67}\text{Ga}_{0.2}\text{Se}_{1.08}$ and $\text{Cu}_{1.0}\text{In}_{0.75}\text{Ga}_{0.16}\text{Se}_{0.87}$ at 0.1 and 0.2 μm from the Mo substrate, respectively. The ratio of Se in the as-deposited film is lower than that of the CIGSe powder. The CIGSe film may have been oxidized by the local heat and carrier gas (air) during the kinetic spray process. To determine the extent of the oxidation, further analysis of the O content in the CIGSe film was conducted. In Fig. 6(b), the results of elemental analysis are shown, performed by measuring EDS at the top and bottom (near the Mo interface) of the CIGSe film, correlating to spectrum 1 and 2, respectively. The EDS spectra at both points indicate the presence of O, but it is more prevalent at the top of the CIGSe film. CIGSe films should be O-free to attain better efficiency. Thus, H_2S treatment is necessary in order to remove the O within the film. The heat treatment and post-treatment characterization of the film are discussed in the following section.

3.4. Analysis of CIGSSe film after post-annealing process

As mentioned in the experimental section, the final CIGSSe film is obtained after a two-step annealing of the as-deposited CIGSe film fabricated by the kinetic spray process. The first annealing step is sulfurization to produce a $\text{Cu}(\text{InGa})\text{S}_2$ (CIGS) film, eliminating the O from the as-deposited CIGSe film. Next, selenization is performed to promote appropriate grain growth in the CIGSSe film and control the bandgap energy. Fig. 7 depicts top-view and cross-sectional SEM micrographs of the (a) as-deposited CIGSe film, (b) sulfurized CIGS film, and (c) selenized CIGSSe film. The as-deposited

CIGSe film in Fig. 7(a) is crack-free and has a thickness of 1.6 μm after six spray passes. The compacted and fractured CIGSe particles are stacked together to form a dense film without damaging the Mo substrate. Fig. 7(b) shows an SEM image of the film after the sulfurization process was performed at 500 $^\circ\text{C}$ for 20 min. After sulfurization, the thickness of the film is unchanged. The surface and cross-sectional view of the film after selenization is shown in Fig. 7(c). The substitution of Se into the CIGS film causes volume expansion; voids are observed in the CIGSSe thin film as a result. A MoSe_2 layer of ~ 0.3 μm thickness is formed at the interface of the CIGSSe film and Mo substrate.

Fig. 8(a) shows the XRD patterns of the sulfurized and selenized CIG(S)Se films. The (112) face orientation, confirmed from the major peak at $2\theta = 26.9^\circ$, indicates the formation of the general chalcopyrite structure of the CIGSe film. The (112) peak of the sulfurized CIGS film is located at $2\theta = 27.93^\circ$ (JCPDS #27-0159). This peak is shifted to a higher angle than that of the CIGSe powder and the as-deposited CIGSe film because of the substitution of Se with S. The selenized CIGSSe film pattern displays two peaks at $2\theta = 27.16^\circ$ and $2\theta = 28.09^\circ$. The strong peak at 27.16° correlates to the typical (112) orientation of CIGSSe, while the weak peak at $2\theta = 28.09^\circ$ indicates the formation of CIGS. In selenization, most S in the CIGS film was substituted with Se; however, some remains in the form of CIGS. The peak at $2\theta = 31.3^\circ$ is attributed to the formation of MoSe_2 [41,42]. This MoSe_2 peak is consistent with the MoSe_2 layer shown in Fig. 7(c).

To confirm the composition of CIGSSe, Auger electron spectroscopy (AES) was performed on the final CIGSSe/CdS/*i*-ZnO/*n*-ZnO/grid layer-structured device, with analysis results presented in Fig. 8(b). The depth profile reveals no impurities in the film. The C layer detected in many other studies was not found in the film fabricated in this study. O is present only in the ZnO region. From

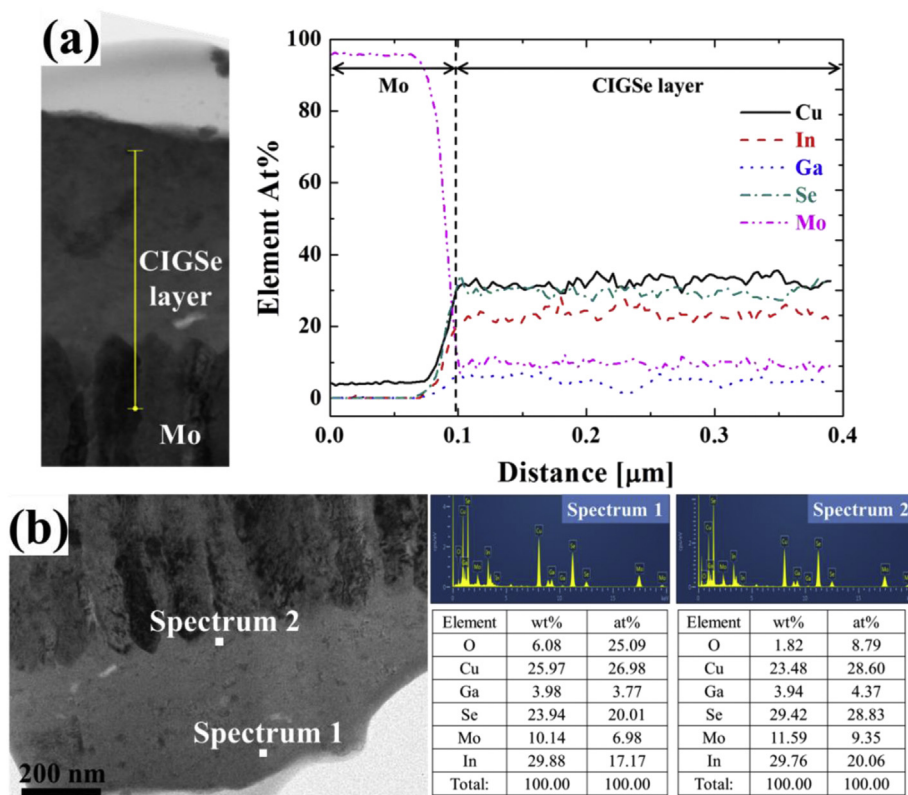


Fig. 6. (a) Cross-sectional image of as-deposited CIGSe film on Mo substrate by focused ion beam (FIB) imaging and energy-dispersive X-ray spectroscopy (EDS) depth profiles of elements, (b) FIB-SEM image and EDS analysis from top and bottom of CIGSe film.

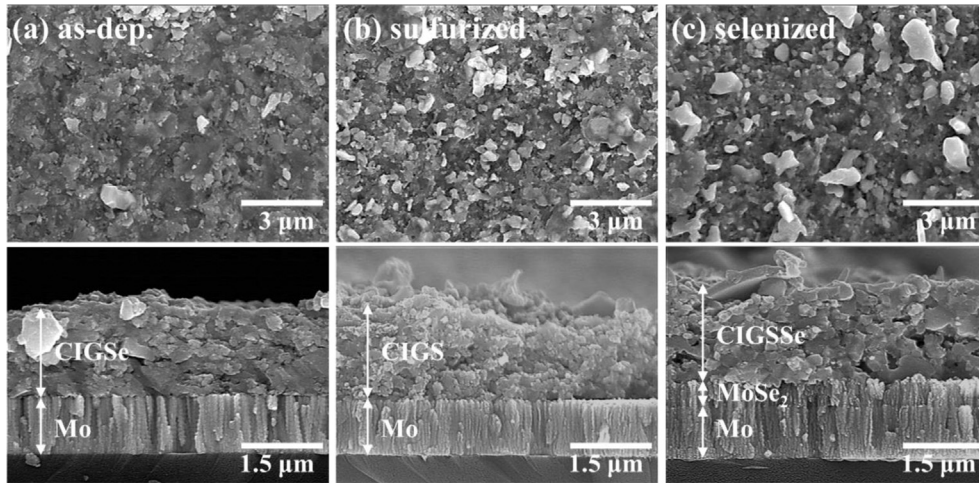


Fig. 7. Top-view (top row) and cross-sectional (bottom row) SEM images of the (a) as-deposited CIGSe film, (b) sulfurized CIGS film, and (c) selenized CIGSSe film.

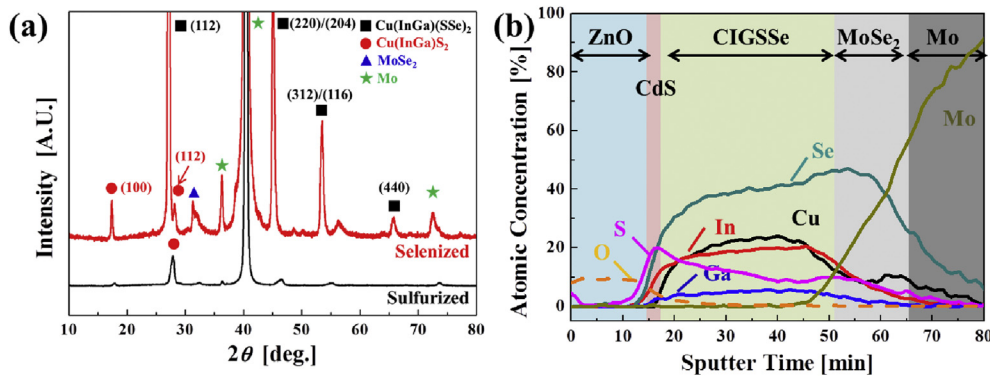


Fig. 8. (a) XRD data of sulfurized and selenized films and (b) AES data of CIGSSe device.

the AES depth profile, in the upper layer, the increased S concentration is a result of the CdS processing and is present throughout the film. The remaining S is in agreement with the XRD data shown in Fig. 8(a). The average Cu and Ga ratios in the middle layer are 0.90 and 0.21, respectively. In the bottom layer, the concentration of Se and Mo are increased because of the MoSe₂ layer.

The final CIGSSe device is scribed into an active area of 0.46 cm² with an Al grid as the front contact. The current density-voltage (*J*-*V*) characteristic curve of the CIGSSe solar cell is shown in Fig. 9(a). The curve shows a *V*_{oc} of 0.34 V, short-circuit current density (*J*_{sc}) of

21.68 mA/cm², *FF* of 54.92%, and conversion efficiency (*η*) of 4.09%. Fig. 9(b) shows the external quantum efficiency (*EQE*) spectrum of the CIGSSe solar cell device. The *EQE* value is low in general and particularly low for longer wavelengths. The *J*_{sc} calculated from the *EQE* data is 21.2 mA/cm², similar to the value measured by the solar simulator in Fig. 9(a). The bandgap of the CIGSSe device, determined from the long-wavelength region of the *EQE* curve, is estimated to be 1.1 eV using the relation between $[h\nu \cdot \ln(1 - EQE)]^2$ and *hν*, where *h* is Planck's constant and *ν* is the frequency of the solar radiation. The efficiency of CIGSSe device is low compared to those

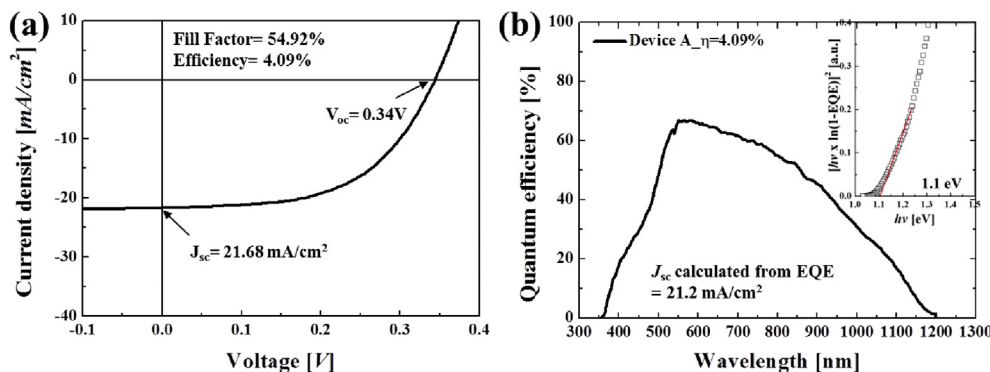


Fig. 9. (a) *J*-*V* curve and (b) *EQE* data of the CIGSSe solar cell.

obtained from cells fabricated in other non-vacuum processes. Table 3 presents the photovoltaic and diode parameters of previously reported CIGSe and CIGSSe solar cells to compare the device characteristics [19,43–45]. Based on the dJ/dV vs. V relation (not shown here), the G value was 8.35 mS/cm^2 for the 4.09%-efficiency device. This is higher than those of other high-efficiency CIG(S)Se solar cells [43–45] while the values of R_s and A of our device are similar to those of other reports. For these reasons, it was inferred that the 4.09%-efficiency device suffered from the low shunt resistance. Strategies for improving the shunt resistance of devices can be divided into the improvement of the absorber-layer morphology and the elimination of unnecessary voids in the film. In terms of morphology, the CIGS thin film with voids and a large roughness value can cause significant shunt currents; the former may allow direct contact between n -ZnO and Mo, while the latter inhibits the conformal coverage of CdS on the CIGS surface. We suspect the voids in the final CIGSSe film (Fig. 7(a)) is the main reason for the high G value.

Based on the above hypothesis, to improve the efficiency of the CIGSe solar cell we focused on improving grain growth in the final CIGSSe film. Increased grain size increases the film density during selenization, thereby reducing the presence of voids.

CuSe is a well-known liquid-phase flux with a low melting point $T_m = 523 \text{ }^\circ\text{C}$. The flux has been widely used to increase the grain size and surface smoothness in CIGSe thin films [37,38,46–48]. Studies on the beneficial impact on grain growth of CuSe have been performed, verifying that the impact results from the improved mobility of the constituent atoms in the liquid phase [37]. Previously, it was demonstrated that the addition of CuSe by physical vapor deposition effectively promoted both grain growth and sintering of CIGSe grains [49]. In a non-vacuum process, Seo et al. [48] used the low-melting-point CuSe phase to generate high-performance dense absorber layers. These reports have shown that CuSe can significantly improve grain growth. We employed the same strategy to enhance grain growth in our CIGSSe films, as described in the next section.

3.5. Modified CIGSSe film deposition process with additional Cu layer

We prepared a bi-layered film composed of a Cu layer and the sulfurized CIGS layer fabricated by kinetic spraying, as shown in Fig. 10(a) and (b). The Cu layer of ~ 300 – 350 nm thickness was deposited on the CIGS layer using Cu powder of $0.8 \text{ }\mu\text{m}$ in size (Alfa Aesar, 99.9%) by kinetic spraying. The CuSe phase was formed by selenization at $550 \text{ }^\circ\text{C}$. The temperature used for selenization approaches the melting temperature of the CuSe phase. Fig. 10(c) and (d) show top- and side-view SEM images of the KCN-etched CIGSSe film after the selenization process. Potassium cyanide (KCN) can be used to selectively remove CuSe phases from CIGSSe thin films [39,50]. Before KCN treatment, the CIGSSe film was rich in Cu/III at 1.49%, as determined by EDS. After KCN treatment for 30 s, the KCN-etched CIGSSe film showed a decrease in Cu/III concentration to 0.89%. The SEM images clearly demonstrate the increased grain

growth in the KCN-etched CIGSSe film after selenization. The images show a significant increase in the grain size of CIGSSe as compared to that seen in Fig. 7(c). The film density increased substantially and the thickness decreased when CuSe was added. While comparing Fig. 10(b) and (d), the film top surface is flattened and smooth after the film densification process via selenization. This implies that CuSe in the CIGSSe film is crucial in promoting CIGSSe grain growth.

The XRD spectra of the selenized CIGSSe film (film A) in Fig. 7(c) and the KCN-etched CIGSSe film selenized from the Cu-coated CIGS film (film B) in Fig. 10(d) are shown in Fig. 11(a). No XRD peaks corresponding to CuSe compounds are observed in the pattern from film B, because they are less likely to form in the Cu-poor conditions induced by KCN treatment. The XRD pattern of film B is sharpened after selenization, indicating growth in the crystalline size of the grains. From the Debye-Scherrer relation, the crystallite size of film B is 29.4 nm . Based on these results, film B has a higher crystallinity than film A, as presented in Table 2. The AES analysis of device B is presented in Fig. 11(b). The average Cu and Ga ratios in the middle layer are 0.82 and 0.28, respectively. After KCN treatment, the concentrations of Cu and Se are slightly decreased in the front CIGSSe layer. A typical MoSe_2 layer is located near the Mo substrate.

Device B achieves a device performance of 5.49% efficiency, as shown in Fig. 12(a). This is significantly higher than that presented in Fig. 9(a). Device B shows a higher V_{oc} of 0.488 V and a slightly lower J_{sc} value compared to device A. FF for device B is 59.99%, exceeding that of device A. The EQE curve in Fig. 12(b) decreases gradually from the maximum point at approximately 530 nm . The value (18.23 mA/cm^2) of J_{sc} calculated from EQE data is similar to the value measured with the solar simulator. The bandgap of device B is estimated to be 1.22 eV , similar to that expected for a CIGSSe solar cell.

Table 3 presents the photovoltaic and diode parameters of device B. Device B shows a higher efficiency because of the increase in FF (improved by 10%) and V_{oc} (improved by 43%) compared to those of device A. The J_o and A values of devices A and B are similar, suggesting that the quality of the main diode itself is similar for the two devices. The FF is increased in device B because of the increased shunt resistance and decreased series resistance. The reduction in shunt resistance can be explained by the improved film density and morphology, as shown in Figs. 7 and 10, as well as the significant reduction of voids. The decrease in series resistance from $1.23 \text{ }\Omega \text{ cm}^2$ to $0.589 \text{ }\Omega \text{ cm}^2$ is attributed to the improved crystallinity of device B.

As described above, the increased V_{oc} of the device built with film B can be partially explained by the increased shunt resistance; however, this is insufficient to explain the significantly large increase in V_{oc} . To determine the reason for the greater increase in V_{oc} , we performed C-V measurements for the devices at 300 K to estimate the carrier densities, as shown in Fig. 13. Assuming that the CIGSSe solar cells have abrupt step junctions, the net carrier concentration and the depletion layer width at $V = 0$ can be related by

Table 3
Comparison of diode parameters and parasitic resistances of solution-processed CIGSSe solar cell.

Ref.	Eff. [%]	FF [%]	V_{oc} [V]	J_{sc} [mA/cm^2]	G [mS/cm^2]	R_s [$\text{ohm}\cdot\text{cm}^2$]	J_o [mA/cm^2]	A
[19]	8.33	55	0.413	36.6	0.23	1.32	3.0×10^{-3}	1.82
[43]	5.87	49.71	0.4	29.44	2.5	1.71	–	2.63
[44]	7.94	58	0.411	33.48	2.1	1.3	–	1.74
[45]	8.75	68.9	0.609	20.86	0.25	2.8	–	–
Device A	4.09	54.92	0.34	21.68	8.35	1.23	7.9×10^{-3}	2.11
Device B	5.49	59.99	0.488	18.73	2.83	0.589	7.8×10^{-3}	2.05

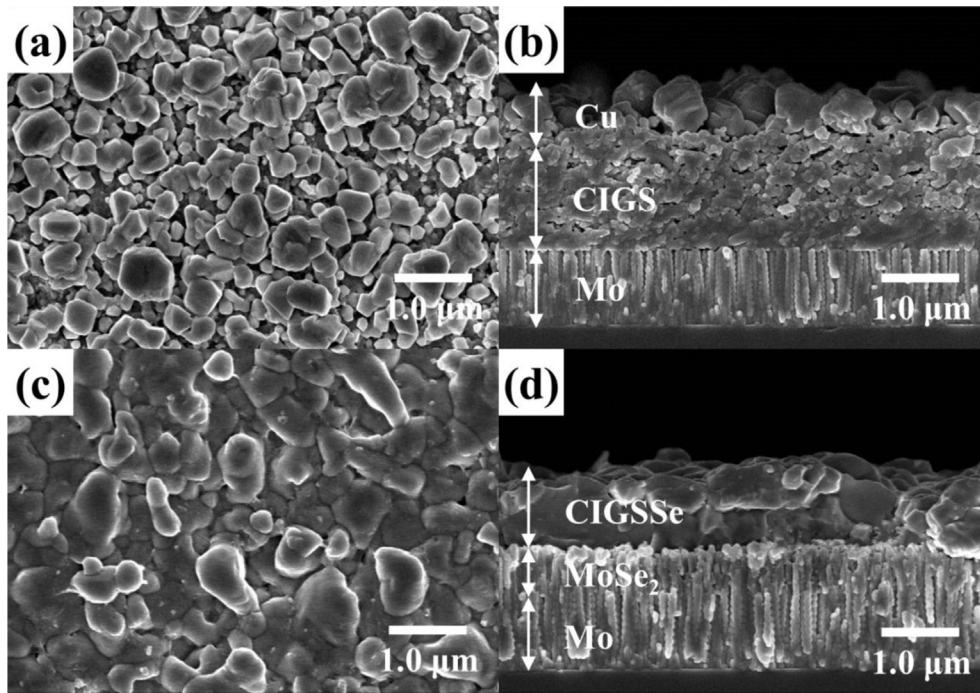


Fig. 10. SEM images of CIGS film with Cu layer before selenization: (a) top view, (b) side view. The KCN-etched CIGSSe film after the selenization process: (c) top view, (d) side view.

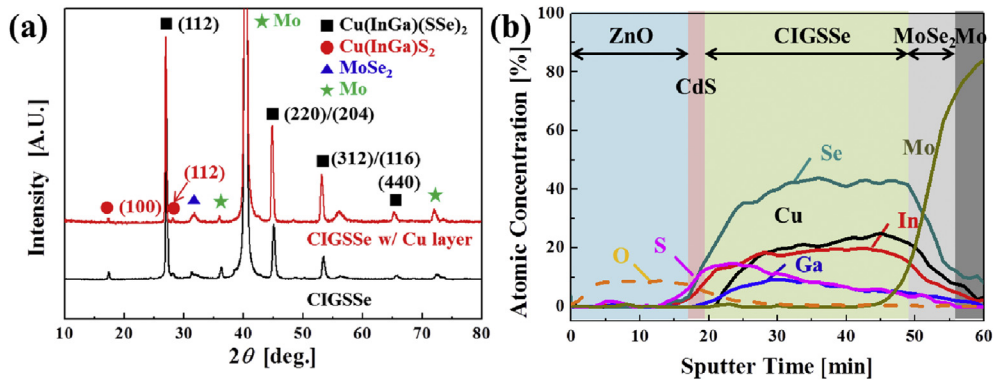


Fig. 11. (a) XRD pattern of the CIGSSe film with and without Cu layer (film A and B, respectively) and (b) AES data from the CIGSSe device with Cu layer (device B).

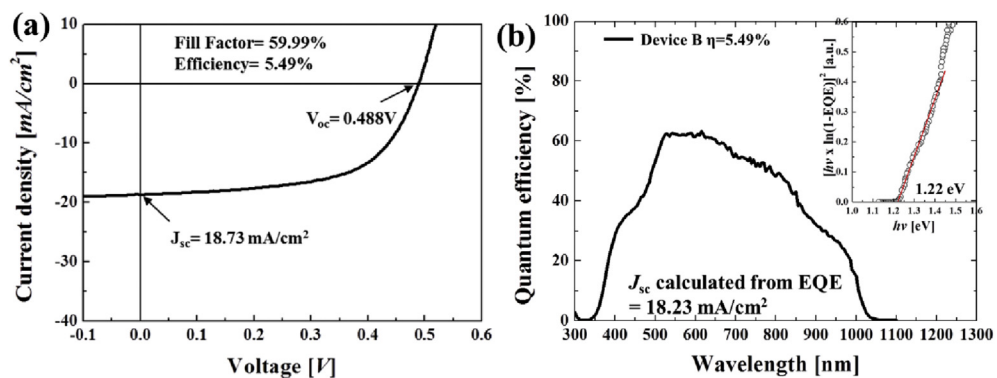


Fig. 12. (a) J-V curve and (b) EQE curve of the device B solar cell (inset: bandgap energy).

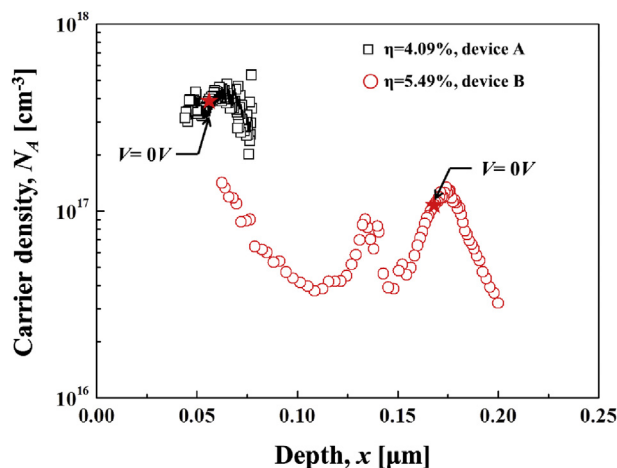


Fig. 13. Carrier density profile, determined from capacitance profiling technique at 300 K.

$$N = \frac{2}{q\epsilon A^2} \frac{dV}{d(1/C^2)} \quad (1)$$

$$\frac{A\epsilon}{W} = C \quad (2)$$

where N is the net carrier concentration, W is the width of the depletion layer, ϵ is the permittivity, A is the area, C is the capacitance, and V is the bias voltage. Compared to device A, B has an increased depletion layer width and decreased carrier density. The values of carrier density in the 4.09% and 5.49%-efficiency devices A and B were determined to be $3.58 \times 10^{17} \text{ cm}^{-3}$ and $3.5 \times 10^{16} \text{ cm}^{-3}$, respectively. These results are higher than the range of typical carrier densities for CIGS solar cells, which is $\sim 10^{15} \text{ cm}^{-3}$ [51]. The Cu/III ratios in device A and B, which determine the density of the shallow acceptor species V_{Cu} , are similar to those of CIGSe devices reported in previous literature. The carrier densities of devices A and B are highly likely to be associated with deep defects. Comparing the two devices in this respect, device B with increased grain size is significantly reduced. This implies the reduction of the deep defect concentration; hence, the reduced recombination is considered an additional reason for the increased V_{oc} of device B.

4. Conclusion

The impact of multiple irregularly shaped particles was simulated to observe the process of formation of dense CIGSe thin films by supersonic spraying. CIGS solar cells were successfully fabricated by the kinetic spray method. The kinetic spray deposited CIGS solar cell efficiency was 4.09%. The deposited CIGSe films were characterized by XRD, TEM, and AES analyses, which confirmed the absence of impurities in the films. Grain growth promoted by CuSe occurred throughout the film during the selenization process. Device B, characterized by increased grain size, exhibited the best efficiency of 5.49% ($FF = 59.99\%$, $V_{\text{oc}} = 0.488 \text{ V}$, $J_{\text{sc}} = 18.73 \text{ mA/cm}^2$). Compared with device A, device B shows a significantly increased V_{oc} and FF . Notably, the CuSe used in the selenization process seems to be significant in improving the quality of the CIGS solar cell absorber layer. To our knowledge, this report is the first record of a kinetic-spray-deposited CIGS solar cell and we believe this is a potential breakthrough in production processing for CIGS solar cells. This attempt can improve the status of CIGS solar cells fabricated by low vacuum processes.

Acknowledgement

This research was supported by Global Frontier Program through the Global Frontier Hybrid Interface Materials (GFHIM) of the National Research Foundation of Korea (NRF) funded by the Ministry of Science, ICT and Future Planning (2013M3A6B1078879) and by the Commercializations Promotion Agency for R&D Outcomes (COMPA) funded by the Ministry of Science, ICT and Future Planning (MISP). S.S. Yoon expresses his appreciation to the Vice Deanship of Scientific Research chairs at King Saud University.

Appendix A. Supplementary data

Supplementary data related to this article can be found at <http://dx.doi.org/10.1016/j.actamat.2016.10.027>.

References

- [1] M. Gossla, W.N. Shafarman, Five-source PVD for the deposition of Cu (In_{1-x}Ga_x)(Se_{1-y}S_y)₂ absorber layers, *Thin Solid Films* 480 (2005) 33–36.
- [2] F. Dhlamini, V. Alberts, Synthesis of homogeneous pentenary chalcopyrite alloys with a classical two-step growth process, *J. Phys. Chem. Solids* 66 (2005) 1880–1882.
- [3] P. Jackson, D. Hariskos, R. Wuerz, O. Kiowski, A. Bauer, T.M. Friedlmeier, M. Powalla, Properties of Cu (In, Ga) Se₂ solar cells with new record efficiencies up to 21.7%, *Phys. Status Solidi* 9 (2014) 28–31.
- [4] C. Eberspacher, C. Fredric, Thin-film CIS alloy PV materials fabricated using non-vacuum, particles-based techniques, *Thin Solid Films* 387 (2001) 18–22.
- [5] F. Lange, Chemical solution routes to single-crystal thin films, *Science* 273 (1996) 903–909.
- [6] Q. Jia, T.M. McCleskey, A. Burrell, Y. Lin, G. Collis, H. Wang, A. Li, S. Foltyn, Polymer-assisted deposition of metal-oxide films, *Nat. Mater* 3 (2004) 529–532.
- [7] M.A. Hossain, M. Wang, K.-L. Choy, Ecofriendly and nonvacuum electrostatic spray-assisted vapor deposition of Cu (In, Ga)(S, Se)₂ thin film solar cells, *ACS Appl. Mater. Interfaces* 7 (2015) 22497–22503.
- [8] M.A. Hossain, Z. Tianliang, L.K. Keat, L. Xianglin, R.R. Prabhakar, S.K. Batabyal, S.G. Mhaisalkar, L.H. Wong, Synthesis of Cu (In, Ga)(S, Se)₂ thin films using an aqueous spray-pyrolysis approach, and their solar cell efficiency of 10.5%, *J. Mater. Chem. A* 3 (2015) 4147–4154.
- [9] S.M. McLeod, C.J. Hages, N.J. Carter, R. Agrawal, Synthesis and characterization of 15% efficient CIGS solar cells from nanoparticle inks, *Prog. Photovolt. Res. Appl.* 23 (2015) 1550–1556.
- [10] M. Kaelin, D. Rudmann, F. Kurdesau, H. Zogg, T. Meyer, A.N. Tiwari, Low-cost CIGS solar cells by paste coating and selenization, *Thin Solid Films* 480 (2005) 486–490.
- [11] S. Ahn, C. Kim, J.H. Yun, J. Gwak, S. Jeong, B.-H. Ryu, K. Yoon, CuInSe₂ (CIS) thin film solar cells by direct coating and selenization of solution precursors, *J. Phys. Chem. C* 114 (2010) 8108–8113.
- [12] T.K. Todorov, O. Gunawan, T. Gokmen, D.B. Mitzi, Solution-processed Cu (In, Ga)(S, Se)₂ absorber yielding a 15.2% efficient solar cell, *Prog. Photovolt. Res. Appl.* 21 (2013) 82–87.
- [13] D.B. Mitzi, M. Yuan, W. Liu, A.J. Kellock, S.J. Chey, V. Deline, A.G. Schrott, A high-efficiency solution-deposited thin-film photovoltaic device, *Adv. Mater* 20 (2008) 3657–3662.
- [14] D.B. Mitzi, Solution processing of chalcogenide semiconductors via dimensional reduction, *Adv. Mater* 21 (2009) 3141–3158.
- [15] D.B. Mitzi, M. Yuan, W. Liu, A.J. Kellock, S.J. Chey, L. Gignac, A.G. Schrott, Hydrazine-based deposition route for device-quality CIGS films, *Thin Solid Films* 517 (2009) 2158–2162.
- [16] E. Lee, S.J. Park, J.W. Cho, J. Gwak, M.-K. Oh, B.K. Min, Nearly carbon-free printable CIGS thin films for solar cell applications, *Sol. Energ. Mat. Sol. Cells* 95 (2011) 2928–2932.
- [17] S.J. Park, J.W. Cho, J.K. Lee, K. Shin, J.H. Kim, B.K. Min, Solution processed high band-gap CuInGaSe₂ thin film for solar cell applications, *Prog. Photovolt. Res. Appl.* 22 (2014) 122–128.
- [18] L.A. Eldada, P. Hersh, B.J. Stanbery, Solution-deposited CIGS thin films for ultra-low-cost photovoltaics, *Proc. SPIE* (2010) 77710–77714.
- [19] Y.S. Lim, H.-S. Kwon, J. Jeong, J.Y. Kim, H. Kim, M.J. Ko, U. Jeong, D.-K. Lee, Colloidal solution-processed CuInSe₂ solar cells with significantly improved efficiency up to 9% by morphological improvement, *ACS Appl. Mater. Interfaces* 6 (2013) 259–267.
- [20] J. Akedo, Room temperature impact consolidation (RTIC) of fine ceramic powder by aerosol deposition method and applications to microdevices, *J. Therm. Spray. Technol.* 17 (2008) 181–198.
- [21] J.-J. Park, J.-G. Lee, S.C. James, S.S. Al-Deyab, S. Ahn, S.S. Yoon, Thin-film metallization of CuInGaSe₂ nanoparticles by supersonic kinetic spraying, *Comput. Mater. Sci.* 101 (2015) 66–76.
- [22] D. Journal of Vacuum Science and Technology AGilmore R. Dykhuizen,

- R. Neiser, M. Smith, T. Roemer, Particle velocity and deposition efficiency in the cold spray process, *J. Therm. Spray. Technol.* 8 (1999) 576–582.
- [23] T. Stoltenhoff, H. Kreye, H. Richter, An analysis of the cold spray process and its coatings, *J. Therm. Spray. Technol.* 11 (2002) 542–550.
- [24] A. Alkhimov, V. Kosarev, S. Klinkov, The features of cold spray nozzle design, *J. Therm. Spray. Technol.* 10 (2001) 375–381.
- [25] B. Jodoin, Cold spray nozzle mach number limitation, *J. Therm. Spray. Technol.* 11 (2002) 496–507.
- [26] J.J. Park, D.Y. Kim, J.G. Lee, D. Kim, J.H. Oh, T.Y. Seong, M.F. Hest, S.S. Yoon, Superhydrophilic transparent titania films by supersonic aerosol deposition, *J. Am. Ceram. Soc.* 96 (2013) 1596–1601.
- [27] J.-J. Park, D.-Y. Kim, S.S. Latthe, J.-G. Lee, M.T. Swihart, S.S. Yoon, Thermally induced superhydrophilicity in TiO₂ films prepared by supersonic aerosol deposition, *ACS Appl. Mater. Interfaces* 5 (2013) 6155–6160.
- [28] J.-J. Park, D.-Y. Kim, J.-G. Lee, Y.-H. Cha, M.T. Swihart, S.S. Yoon, Supersonic aerosol-deposited TiO₂ photoelectrodes for photoelectrochemical solar water splitting, *RSC Adv.* 4 (2014) 8661–8670.
- [29] D.-Y. Kim, B.N. Joshi, J.-J. Park, J.-G. Lee, Y.-H. Cha, T.-Y. Seong, S.I. Noh, H.-J. Ahn, S.S. Al-Deyabe, S.S. Yoon, Graphene–titania films by supersonic kinetic spraying for enhanced performance of dye-sensitized solar cells, *Ceram. Int.* 40 (2014) 11089–11097.
- [30] M. Katayama, S. Toda, S. Kibe, Numerical simulation of space debris impacts on the Whipple shield, *Acta Astronaut.* 40 (1997) 859–869.
- [31] D.M. Chun, S.H. Ahn, Deposition mechanism of dry sprayed ceramic particles at room temperature using a nano-particle deposition system, *Acta mater.* 59 (2011) 2693–2703.
- [32] J. Akedo, Aerosol deposition of ceramic thick films at room temperature: densification mechanism of ceramic layers, *J. Am. Ceram. Soc.* 89 (2006) 1834–1839.
- [33] G. Bae, K. Kang, J.-J. Kim, C. Lee, Nanostructure formation and its effects on the mechanical properties of kinetic sprayed titanium coating, *Mater. Sci. Eng. A* 527 (2010) 6313–6319.
- [34] J.-G. Lee, D.-Y. Kim, B. Kang, D. Kim, S.S. Al-Deyab, S.C. James, S.S. Yoon, Thin film metallization by supersonic spraying of copper and nickel nanoparticles on a silicon substrate, *Comput. Mater. Sci.* 108 (2015) 114–120.
- [35] M. Lebedev, J. Akedo, K. Mori, T. Eiju, Simple self-selective method of velocity measurement for particles in impact-based deposition, *J. Vac. Sci. Technol. A* 18 (2000) 563–566.
- [36] T. Tinoco, C. Rincón, M. Quintero, G.S. Pérez, Phase diagram and optical energy gaps for CuIn_yGa_{1-y}Se₂ alloys, *Phys. Status Solidi* 124 (1991) 427–434.
- [37] S. Ahn, K. Kim, A. Cho, J. Gwak, J.H. Yun, K. Shin, S. Ahn, K. Yoon, CuInSe₂ (CIS) thin films prepared from amorphous Cu–In–Se nanoparticle precursors for solar cell application, *ACS Appl. Mater. Interfaces* 4 (2012) 1530–1536.
- [38] X.L. Zhu, Y.M. Wang, Z. Zhou, A.M. Li, L. Zhang, F.Q. Huang, 13.6%-efficient Cu(In,Ga)Se₂ solar cell with absorber fabricated by RF sputtering of (In,Ga)₂Se₃ and CuSe targets, *Sol. Energ. Mat. Sol. Cells* 113 (2013) 140–143.
- [39] Q. Guo, S.J. Kim, M. Kar, W.N. Shafarman, R.W. Birkmire, E.A. Stach, R. Agrawal, H.W. Hillhouse, Development of CuInSe₂ nanocrystal and nanoring inks for low-cost solar cells, *Nano Lett.* 8 (2008) 2982–2987.
- [40] M. Lebedev, J. Akedo, A. Iwata, S. Sugimoto, K. Inomata, NiZnCu ferrite thick film with nano scale crystallites formed by the aerosol deposition method, *J. Am. Ceram. Soc.* 87 (2004) 1621–1624.
- [41] S. Ahn, K.H. Kim, J.H. Yun, K.H. Yoon, Effects of selenization conditions on densification of Cu (In, Ga) Se₂ (CIGS) thin films prepared by spray deposition of CIGS nanoparticles, *J. Appl. Phys.* 105 (2009) 113533.
- [42] T. Wada, N. Kohara, S. Nishiwaki, T. Negami, Characterization of the Cu (In, Ga) Se₂/Mo interface in CIGS solar cells, *Thin Solid Films* 387 (2001) 118–122.
- [43] A. Cho, S. Ahn, J.H. Yun, Y.-J. Eo, H. Song, K. Yoon, Carbon layer reduction via a hybrid ink of binary nanoparticles in non-vacuum-processed CuInSe₂ thin films, *Sol. Energ. Mat. Sol. Cells* 110 (2013) 126–132.
- [44] S. Ahn, Y.J. Choi, K. Kim, Y.J. Eo, A. Cho, J. Gwak, J.H. Yun, K. Shin, S.K. Ahn, K. Yoon, Amorphous Cu–In–S nanoparticles as precursors for CuInSe₂ thin-film solar cells with a high efficiency, *ChemSusChem* 6 (2013) 1282–1287.
- [45] G. Wang, S. Wang, Y. Cui, D. Pan, A novel and versatile strategy to prepare metal–organic molecular precursor solutions and its application in Cu (In, Ga)(S, Se)₂ solar cells, *Chem. Mater* 24 (2012) 3993–3997.
- [46] R. Klenk, T. Walter, H.W. Schock, D. Cahen, A model for the successful growth of polycrystalline films of CuInSe₂ by multisource physical vacuum evaporation, *Adv. Mater* 5 (1993) 114–119.
- [47] J. Tuttle, M. Contreras, M. Bode, D. Niles, D. Albin, R. Matson, A. Gabor, A. Tennant, A. Duda, R. Noufi, Structure, chemistry, and growth mechanisms of photovoltaic quality thin-film Cu (In, Ga) Se₂ grown from a mixed-phase precursor, *J. Appl. Phys.* 77 (1995) 153–161.
- [48] Y.-H. Seo, B.-S. Lee, Y. Jo, H.-G. Kim, Y. Choi, S. Ahn, K. Yoon, K. Woo, J. Moon, B.-H. Ryu, Facile microwave-assisted synthesis of multiphase CuInSe₂ nanoparticles and role of secondary CuSe phase on photovoltaic device performance, *J. Phys. Chem. C* 117 (2013) 9529–9536.
- [49] T. Wada, Y. Matsuo, S. Nomura, Y. Nakamura, A. Miyamura, Y. Chiba, A. Yamada, M. Konagai, Fabrication of Cu (In, Ga) Se₂ thin films by a combination of mechanochemical and screen-printing/sintering processes, *Phys. Status Solidi* 203 (2006) 2593–2597.
- [50] T.-P. Hsieh, C.-C. Chuang, C.-S. Wu, J.-C. Chang, J.-W. Guo, W.-C. Chen, Effects of residual copper selenide on CuInGaSe₂ solar cells, *Solid-State Electron.* 56 (2011) 175–178.
- [51] J.T. Heath, J.D. Cohen, W.N. Shafarman, Bulk and metastable defects in CuIn_{1-x}Ga_xSe₂ thin films using drive-level capacitance profiling, *J. Appl. Phys.* 95 (2004) 1000–1010.